

A Gauss-Seidel Iteration Scheme for Reference-Free 3-D Histological Image Reconstruction

Simone Gaffling*, Volker Daum, Stefan Steidl, Andreas Maier, Harald Köstler and Joachim Hornegger, *Member, IEEE*

Abstract—Three-dimensional (3-D) reconstruction of histological slice sequences offers great benefits in the investigation of different morphologies. It features very high-resolution which is still unmatched by in-vivo 3-D imaging modalities, and tissue staining further enhances visibility and contrast. One important step during reconstruction is the reversal of slice deformations introduced during histological slice preparation, a process also called image unwarping. Most methods use an external reference, or rely on conservative stopping criteria during the unwarping optimization to prevent straightening of naturally curved morphology. Our approach shows that the problem of unwarping is based on the superposition of low-frequency anatomy and high-frequency errors. We present an iterative scheme that transfers the ideas of the Gauss-Seidel method to image stacks to separate the anatomy from the deformation. In particular, the scheme is universally applicable without restriction to a specific unwarping method, and uses no external reference. The deformation artifacts are effectively reduced in the resulting histology volumes, while the natural curvature of the anatomy is preserved. The validity of our method is shown on synthetic data, simulated histology data using a CT data set and real histology data. In the case of the simulated histology where the ground truth was known, the mean Target Registration Error (TRE) between the unwarped and original volume could be reduced to less than 1 pixel on average after 6 iterations of our proposed method.¹

Index Terms—3-D Histology, Reconstruction, Registration, Reference-free, Gauss-Seidel

I. INTRODUCTION

A. Biomedical Motivation

Imaging modalities that are able to directly visualize 3-D objects, e.g., μ -CTs/MRs, only recently achieve resolution values of about 0.7 μm . However, they still do not match

Asterisk indicates corresponding author.

S. Gaffling (email: simone.gaffling@cs.fau.de), S. Steidl, A. Maier and J. Hornegger are with the Pattern Recognition Lab, Department of Computer Science, Friedrich-Alexander-University of Erlangen Nuremberg (FAU), Martensstr. 3, 91058 Erlangen, Germany

V. Daum is with Chimaera GmbH, Am Weichselgarten 7, 91058 Erlangen, Germany

H. Köstler is with the Chair of System Simulation, Department of Computer Science, Friedrich-Alexander-University of Erlangen Nuremberg (FAU), Cauerstr. 11, 91058 Erlangen, Germany

S. Gaffling, A. Maier, H. Köstler and J. Hornegger are members of the Graduate School in Advanced Optical Technologies (SAOT), Paul-Gordan-Str. 6, 91052 Erlangen, Germany

¹Copyright (c) 2010 IEEE. Personal use of this material is permitted. However, permission to use this material for any other purposes must be obtained from the IEEE by sending a request to permissions@ieee.org.

the high resolution of conventional light microscopes, and lack the possibility to stain structures of interest to enhance the contrast and thus their visibility. Therefore, the investigation of histological image sequences to gain insight into 3-D morphological structures is still a regular task in biomedical laboratories.

Especially when the spatial relationship between anatomical structures and their progression has to be investigated, a significant disadvantage is that the spatial connectivity of structures is lost during histological slice preparation. Envisioning a 3-D structure from an image sequence is challenging, especially for large data sets. In contrast to that, looking at a 3-D object from different angles helps to infer spatial relationships very fast. In addition, the extraction of quantitative values is often easier and more reliably done using volumetric data.

A possibility to combine the advantages of 3-D imaging with the staining and high-resolution properties of light microscopy is to create a 3-D reconstruction of the original tissue from the histological image sequence. Restoring the anatomy such that it closely recovers the original in-vivo tissue sample can tremendously facilitate the perception of the morphology and spatial relations. As both the slice preparation and digitizing process introduce artifacts, however, merely stacking the 2-D images is not an option. The reconstruction routine – consisting of all processing steps that are necessary to achieve the reconstruction – is therefore closely related to the histological slice preparation process.

B. Histological Slice Preparation and Preprocessing

To generate a sequence of digital histology images, an extensive procedure is necessary. After extraction, the tissue is fixed and embedded into a synthetic material. Depending on the specific synthetic that is used, this block is then cut into slices, typically with a thickness of about 0.5–20 μm . The slice thickness is usually chosen such that the structure of interest varies slowly with the number of sections, to be able to investigate the structure morphology. After the slices were placed on an object plate, the embedding synthetic is removed. Then, the histological staining is applied, typically a series of chemical treatments with histological dyes, alcohol and distilled water at different temperatures. This procedure

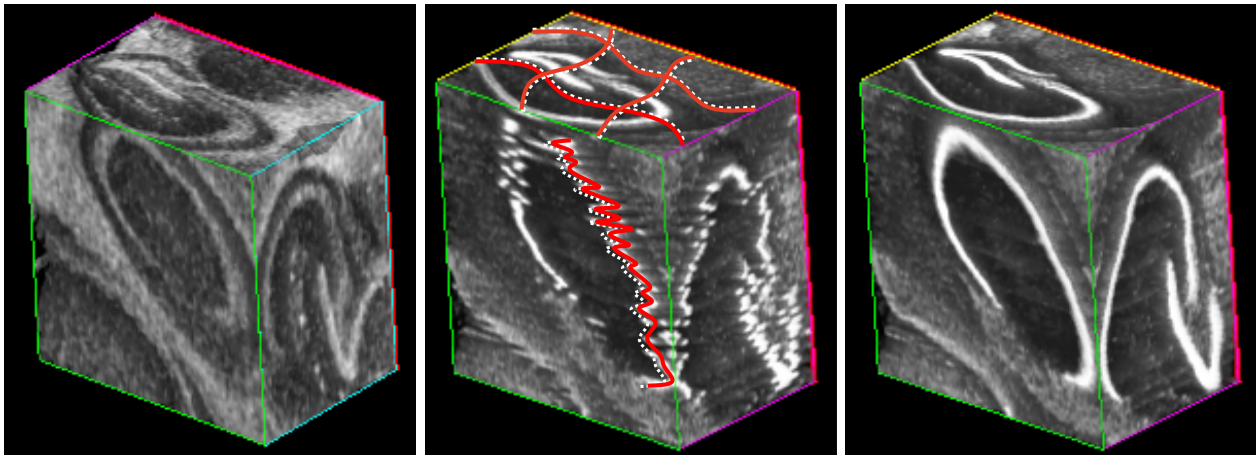


Figure 1: Left: Smooth, undisturbed volume rendering of the hippocampal region showing the pyramidal layer and dentate gyrus of a T2*-weighted MRI of a mouse brain [1]. Middle: Structures after stacking the rigidly aligned, but still deformed histological slices [2]. Deformations (red/dashed) within the slice plane show low to moderate curvature, while the deformation of the anatomy along the stack corresponds to high-frequency errors. Right: Reconstruction result using our approach. For references regarding color be referred to the web version of our article.

greatly enhances the visibility of the anatomical structures of interest. Finally the stained slices are viewed under a microscope, and digitized using a microscope-mounted camera. Alternatively semi-automatic systems capable of focusing, capturing and stitching several partial images to the final image covering the object of interest are used.

Unfortunately, each of the aforementioned steps introduces artifacts which degrade the quality of the resulting digital images representing the original tissue slice. While, e.g., tissue shrinking during fixation and embedding is assumed to be small and therefore negligible, other artifacts have to be addressed to ensure that the 3-D reconstruction result is as similar to the original in-vivo tissue sample as possible. Therefore, most reconstruction methods include a preprocessing stage, linear alignment as well as a strategy to reverse the slice deformations.

Consequently, the first step is to normalize the slice intensities. Inconsistent lighting conditions during digitizing lead to an intensity bias on every image. They are usually brighter in the center region than at the borders of the image, which has to be corrected [3], [4]. Varying conditions during the staining procedure lead to differently distinct colorings of the tissue slices, such that the same tissue class shows a different color in different images. Different procedures were suggested to normalize these intensities [5], [6], [7].

The most severe artifacts, however, stem from the cutting procedure, as it introduces tissue deformations - or warps - within the slice plane, and generally destroys the spatial relationship between slices and thus the connectivity of the original anatomy.

Therefore, one crucial step in reconstruction is the global alignment of the slices. Its task is to rigidly transform the sections such that translational offset and rotation differences between slice images are compensated. This will restore the global true shape of the original

tissue sample, which is a prerequisite for an accurate reconstruction. Global shape here means the large-scale overall form of the structure of interest, not accounting for the smaller-scale distortions still contained in the images. In the absence of ground-truth reference information, there is unfortunately no guarantee that the calculated global shape will represent the actual shape.

Still, there are different approaches how to achieve good results. First, the actual structure of interest is quite often embedded in surrounding tissue, which can regularize the rigid registration of slices such that the global shape corresponds to the real tissue shape without the need of further correction. A second possibility is the use of an atlas image as external reference, which might be helpful to recover a realistic global shape. Sometimes, fiducial markers were used for alignment. Finally, due to the lower number of degrees of freedom in rigid registration as compared to non-rigid registration, manual refinement of an automatically created rigidly registered volume is also an option. You can find more information about this crucial step in the references of section I-D

Our article focuses on a strategy for reversal of slice deformations, also called image unwarping. We therefore assume for the sake of this article that all previous steps, i.e., preprocessing and linear alignment, have already been taken. For more detailed information about these steps, also refer to [8], [9], [10], [11] and references therein.

C. Problem Definition

To justify the approach we are taking for slice unwarping, one has to take a closer look at the problem at hand. When cutting the tissue into slices, section thickness is chosen such that the structure of interest varies slowly with the number of sections. If done otherwise, the shape of the structure might be undersampled, and any investigation of the morphology obsolete. The natural morphological

structure along the stack is therefore comparable to a function with low or moderate spatial frequency, sampled at the slice locations.

In addition, depending on the robustness of the tissue and diligence during the preparation process, the slice preparation leads to artifacts such as tears, foldings and gaps corresponding to sharp local deformations. While we included an elaboration of the impact and treatment of these defects later in this article, the focus of our work are the more global, smooth in-plane deformations that are inevitably present in the final tissue slices.

As these smooth deformations are different for each slice, merely stacking the rigidly registered slice images leads to high-frequency disturbances of the original anatomy along the stack. They present the main reason linearly aligned reconstructions appear jagged and discontinuous.

Along the stack, the slowly oscillating “anatomic function” is basically superimposed with the highly oscillating disturbances due to the slice deformations. Figure 1 visually illustrates this fact. The actual problem one has to solve in histological image unwarping is then to eliminate the high-frequency components from the deformation while preserving the low frequency components representing the natural anatomy. This has to be achieved by unwarping the individual histology images, emulating the smooth in-plane deformation imposed during cutting,

D. Related Work

3-D reconstruction of slice images has a long tradition, going back as far as 1883 [12]. The invention and steady advancement of computer technology enabled the development of more and more sophisticated methods for spatial restoration of disassembled anatomical structures. For an extensive review of the history and different methodologies developed for 3-D histological image reconstruction see [8] and [13].

Many techniques rely on prior knowledge about the undeformed, original structure to guide the reconstructions. How this knowledge is incorporated differs, and includes mostly fiducial markers (e.g., in [14], [15]), blockface photographs (e.g., [16], [17]), or volume images acquired using 3-D imaging modalities (e.g., [18], [19]). While external knowledge undeniably helps to restore the original shape and connectivity, it also has to be stated that this information is often not available. The reasons for this are manifold.

Blockface photographs require the acquisition of an image of the unstained surface of the embedded tissue block. On the one hand this is tedious, as this has to be done for each individual slice, interrupting the regular workflow. On the other hand, this is only possible for certain types of staining, as it has to be applied on-the-fly on each individual slice after one slice is cut from the block. Prior acquisition of a volume image, e.g., from a μ -CT/ μ -MR, is often not possible as the devices are not available, and the resolution is mostly still too small to visualize the

relevant structures. Apart from that, histological staining might be necessary to make the structures of interest visible in the first place, which of course is not possible in this case. As stated above, while the usage of an atlas as external reference may be sufficient to recover a realistic global shape, it certainly would not be appropriate for performing a non-rigid correction. Last, there is a large pool of highly valuable historical slice sequences, where naturally a reference is not available. Any reconstruction method that aims to reconstruct one of these sequences has to be able to forgo such a reference.

There have been some attempts to achieve an anatomically sound reconstruction without the use of an external reference. Braumann et al. [20] use a series of three registration steps for reconstruction. After initial rigid alignment, the slices are registered using a polynomial non-linear registration, and later the alignment is refined using a curvature-based registration approach. Ju et al. [2] propose to calculate pairwise warps between adjacent, bilaterally filtered slices, and the final warp for an image is then given by a binomially weighted sum of the warps from that image to images in a certain neighborhood of size d . Wirtz et al. [21] optimize an objective function measuring the elastic potential of the deformation field, which is extended for image stacks. Similarly, Schmitt et al. [8] achieve global alignment using a principal axes transform and optimizing rotation and shearing. This is followed by an elastic non-rigid registration routine. Chakravarty et al. developed two different approaches. In [22] they used slice-to-slice non-linear registration, minimizing the mean distance between segmented contours. Their second approach [23] extends their previous work, and similarly to Ju et al. [2], uses an average deformation field calculated from the deformations to the four predecing and four succeeding slices. Pitiot et al. [24], [25] use block-matching to estimate a displacement field between neighboring images. They then use regularization with adaptable rigidity, incorporating also the geometry and topology of the images. The image stack is processed starting with a manually chosen reference slice. Bađci et al. [26] propose to map the histological images into a feature space called edgeness space, and use elastic registration of the slices in this feature space, starting with an automatically chosen best reference slice. Scheibe et al. [27] use non-rigid registration based on an intensity similarity measure and regularization of the deformation based on the optical flow. Slices are registered to their respective predecessor in a forward-backward iteration scheme. Finally, Cifor et al. [13] propose a smoothness-driven method, calculating a min-max curvature flow restricted to 2-D planes. From the flow, arbitrarily flexible transformations can be calculated.

E. Contribution

First, we define the goal of histological image unwarping to separate superimposed functions of different frequencies, as stated in section I-C. We introduce a non-rigid registration scheme that transfers the iterative Gauss-Seidel method to images. That way we can reverse the

artificially introduced slice deformations and restore the smooth spatial connectivity of the tissue morphology, while preserving the natural curvature of structures. In particular, we achieve this without the use of an external reference. While most approaches dealing with histological image unwarping present a method for the unwarping method itself, i.e., emulating the deformation, we instead focus on *how this method has to be applied on an image stack* to achieve the desired result. The user is therefore not bound to a specific type of non-rigid registration, but instead is able to use whatever method works best for the data at hand.

F Outline

The article is organized as follows. In section II, we describe the employed methods we use for reference-free histological image reconstruction. First, we explain the non-rigid, non-parametric image registration method we use for image unwarping in Section II-A. We then give a short explanation of the iteration scheme and convergence behavior of the Gauss-Seidel method, which our reconstruction scheme is based on, in Section II-B1. In Section II-C, we transfer the previously described mathematical concepts into the domain of images and image registration, and finalize the section with an algorithmic overview of our approach. Section III describes the data and experiments that were used to evaluate our method, and shows qualitative and quantitative results on simulated and real data. The article is concluded with a summary and discussion in section IV.

II. METHODS

The unwarping strategy of an entire histological image stack requires the reversal of the artificial deformation of each individual section. This process is guided by several assumptions and requirements.

As stated before, one prerequisite for a truthful reconstruction is that the global shape of the original tissue was correctly recovered in the initial linear alignment step. A failed linear alignment of the slices, e.g., a global rotation or tilt, corresponds to a low frequency error. Since our method is specifically targeted at high frequency artifacts, it will not be able to restore errors of the global shape.

Assumptions regarding the slice deformations itself are that they are smooth in accordance with the elasticity of organic material, are restricted to deformations within the plane, and deformations of one slice are independent from deformations of neighboring slices. An additional requirement is that the connectivity and run of anatomical structures along the stack is assumed to be smooth after reversing the deformation of each individual slice. And last, the natural curvature of the anatomy along the stack has to be preserved.

While the assumptions about the nature of the deformations are mostly relevant for unwarping individual slices, the requirements of smooth progression of structures and preservation of the natural curvature demand to take

into account the neighborhood of the sections that are currently processed, or even the entire stack of images, and therefore require global optimization strategies. In fact, a common and well-known problem in histological image reconstruction is known as aperture or banana problem [8], [28], [2], [26]. It stems from the fact that individual treatment of the slices according to the first and second assumption – i.e., reversing the deformation within the slice plane such that the connectivity of structures along the stack is restored and smooth – often lead to results that violate the third criterion, basically straightening the natural curvature. Note that this effect can also occur during the linear alignment of the slices, which is why this step has to be performed with great care. Therefore, it is important to ensure that all assumptions and requirements are simultaneously fulfilled, as this is the only way to achieve an anatomically correct reconstruction of the entire histological image sequence.

A. In-plane Deformations

The most challenging part in histological image reconstruction is the reversal of the tissue slice deformations. Beside the cutting direction during slice preparation – and therefore a possible bias of the deformation in one direction – the individual deformations of slices are considered to be independent of each other. A commonly used strategy to reverse these deformations is 2-D non-rigid registration. It can be used to compensate motion between images such that corresponding content is mapped onto each other. The types of transforms, and the optimization strategies that are used, however, differ significantly, and are often tailored to the data at hand. Similar to [8], we will employ a non-rigid, non-parametric registration formulation in a custom implementation[29].

Mathematically, the aim of a 2-D image registration is to find a mapping $\mathbf{u} : \mathbb{R}^2 \rightarrow \mathbb{R}^2$ between a reference image R and a template image T , such that the deformed template image $T_{\mathbf{u}}(\mathbf{x}) = T(\mathbf{x} - \mathbf{u}(\mathbf{x}))$ is similar to R . The similarity of the images is measured by a distance measure \mathcal{D} , which is minimal if the similarity is maximal. Additionally we require the deformation \mathbf{u} to be constrained in some sense, which in our case means we want it to be smooth according to the elastic deformation of the tissue.

The smoothness is measured by the regularizer \mathcal{R} . All in all, we thus want to solve

$$\mathbf{u}^* = \underset{\mathbf{u}}{\operatorname{argmin}} \mathcal{D}(R, T_{\mathbf{u}}) + \alpha \mathcal{R}(\mathbf{u}) := \operatorname{NPREG}(R, T), \quad (1)$$

where α is a weighting parameter that decides whether we prefer a better match or a smoother deformation. Throughout this article, NPREG is used as an abbreviation for non-rigid, **non-parametric image registration** between images R and T .

As we only have to deal with mono-modal registration problems in this work, we employ the well known sum-of-squared differences (SSD) as distance measure. It is defined as

$$\mathcal{D}_{\text{SSD}}(R, T_{\mathbf{u}}) = \frac{1}{|\Omega|} \int_{\Omega} (R(\mathbf{x}) - T_{\mathbf{u}}(\mathbf{x}))^2 d\mathbf{x},$$

where Ω is the computational domain of the registration and $|\Omega|$ its area. As regularizer we employ the curvature regularization, popularized in [30]:

$$\mathcal{R}_{\text{CURV}}(\mathbf{u}) = \frac{1}{|\Omega|} \int_{\Omega} \|\Delta \mathbf{u}(\mathbf{x})\|_2^2 \, d\mathbf{x}.$$

The curvature regularizer minimizes the norm of the second order derivatives of the deformation field \mathbf{u} , given by the Laplace operator Δ . We choose the curvature regularizer, because it does not penalize affine transformations. This can be an advantage in the context of histological image unwarping, as the non-linear transform between reference and template images might additionally contain an affine component. For a more in-depth discussion please refer to [31], [29] and [32].

This non-rigid registration method gives us a means to generate a deformation field that is in general able to emulate (or therefore reverse) the smooth global deformations that were imposed on the slices during cutting. Although the individual slice deformations are deemed independent from each other, as we do not have an external reference, we need to take the neighborhood into account. The specific deformations can therefore only be calculated when the anatomical smoothness along the stack is considered.

B. Elimination of High-Frequency Errors

As was shown in Figure 1, the deformations within the slice plane lead to high-frequency disturbances of the originally smooth structures along the stack. Mathematically, high frequencies correspond to high curvature, i.e., large values for the second derivative of a function. As stated in section I-C, the problem to solve is therefore to eliminate high-curvature components from a function where low and high curvature components are superimposed. To reverse this, our reconstruction scheme is based on a Gauss-Seidel iteration scheme. We take advantage of the smoothing property of Gauss-Seidel to eliminate the high-frequency deformations of our digital histology volume to restore the original, smooth progression and curvature of the in-vivo anatomical structures. We will first explain the idea and properties we exploit on a fictional 1-D model problem, introducing the iterative Jacobi, weighted Jacobi and Gauss-Seidel methods, and later reformulate the equations in terms of images and deformation fields.

1) *Model Problem:* In the following section we will demonstrate the effect of the employed iterative solution schemes on different frequency components of a given function f when these methods are applied. For this purpose, we assume for the moment that the ideal function $f^* : [0, 1] \rightarrow \mathbb{R}$ we would like to restore given an initial function f has a minimal absolute curvature. In the ideal case, this corresponds to a second-order differential equation

$$f^{*''}(x) = 0 \quad 0 < x < 1 \quad (2)$$

on a domain $\Omega \in (0, 1)$. For simplicity we assume Dirichlet boundary conditions, i.e., boundary values that are known and therefore fixed,

$$f(0) = f(1) = 0.$$

The function domain Ω is first discretized into m subintervals of uniform width $h = 1/m$, resulting in $m + 1$ grid points $x_i = i \cdot h$, $i := \{i \in \mathbb{N} \mid 0 \leq i \leq m\}$. At each of the $m - 1$ interior grid points x_i , the second derivative of f can be expressed by the central-difference approximation

$$f''(x_i) = \frac{f(x_{i-1}) - 2f(x_i) + f(x_{i+1}))}{h^2} \stackrel{!}{=} 0. \quad (3)$$

Eliminating h^2 by multiplication, we solve each i -th equation for the i -th unknown. Every discretized function value can therefore be expressed as linear combination of its neighbors

$$f(x_i) = \frac{1}{2} (f(x_{i-1}) + f(x_{i+1})), \quad (4)$$

and we can generate a vector of discrete values approximating our function,

$$\mathbf{f} = (f(x_1), f(x_2), \dots, f(x_{m-1}))^T = (f_1, f_2, \dots, f_{m-1})^T.$$

Starting with the discretized values $f_i^{(0)}$ of given function f , we can iteratively update these values using Eq. (4), which after t iterations are given by

$$f_i^{(t)} = \frac{1}{2} (f_{i-1}^{(t-1)} + f_{i+1}^{(t-1)}). \quad (5)$$

This can be interpreted such that for the current iteration neighboring values are assumed to be correct, and are used to calculate a better approximation for the grid point in between. All values of \mathbf{f} are either simultaneously or subsequently updated, and the next iteration is started. This iterative scheme is a special form of the well-known Jacobi method [33].

A popular modification of this scheme is to use the updated value of Eq. (5) just as intermediate value $f_{i, \text{interm}}^{(t)}$. The final update value $f_i^{(t)}$ is then a weighted combination of the old function value $f_i^{(t-1)}$ and this intermediate value, i.e.,

$$f_i^{(t)} = (1 - \omega) f_i^{(t-1)} + \omega f_{i, \text{interm}}^{(t)}. \quad (6)$$

Adjusting the weight ω can lead to faster or slower convergence, and can be tailored to the specific type of problem at hand.

To investigate the convergence and smoothing properties, it is useful to look into the methods in matrix notation. Multiplied with -1 for optimization reasons, Eq. (3) is equivalent to a system of linear equations

$$\begin{pmatrix} 2 & -1 & 0 & \cdots \\ -1 & 2 & -1 & \\ 0 & \vdots & \ddots & \\ & & -1 & 2 \end{pmatrix} \begin{pmatrix} f_1 \\ f_2 \\ \vdots \\ f_{m-1} \end{pmatrix} = \begin{pmatrix} 0 \\ 0 \\ \vdots \\ 0 \end{pmatrix}$$

$$\mathbf{A}\mathbf{f} = \mathbf{0}.$$

The symmetric, positive definite Matrix \mathbf{A} is decomposed into its components - diagonal matrix \mathbf{D} , lower and upper

triangular matrices \mathbf{L} and \mathbf{U} - and the iteration scheme of the Jacobi method can be rewritten as

$$\mathbf{f}^{(t)} = \underbrace{\mathbf{D}^{-1}(\mathbf{L} + \mathbf{U})}_{\mathbf{R}} \mathbf{f}^{(t-1)}$$

with iteration matrix \mathbf{R} . For the weighted Jacobi method (Eq. 6), the iteration matrix changes to

$$\mathbf{R}_\omega = (1 - \omega)\mathbf{I} + \omega\mathbf{R}.$$

2) *Smoothing and convergence*: As the iterative Jacobi and Gauss-Seidel methods were invented in the early 19th century, their convergence and smoothing properties are well understood, e.g., compare [34] and references therein. Therefore we will only provide a brief overview about the main parts of the theory related to our problem.

In general, the remaining error of our original model problem (2) after t iterations is defined as the difference between the ground-truth solution \mathbf{f}^* and the current approximation $\mathbf{f}^{(t)}$

$$\mathbf{e} = \mathbf{f}^* - \mathbf{f}^{(t)}.$$

The iteration scheme says that a new approximation is given by

$$\mathbf{f}^{(1)} = \mathbf{R}\mathbf{f}^{(0)}.$$

The real solution \mathbf{f}^* is a fixed point of the iteration process, i.e., $\mathbf{f}^* = \mathbf{R}\mathbf{f}^*$, which means that after convergence, further iterations do not change the solution anymore. The error of the iteration scheme after the first iteration is therefore given by

$$\mathbf{e}^{(1)} = \mathbf{R}\mathbf{e}^{(0)},$$

and after t iterations

$$\mathbf{e}^{(t)} = \mathbf{R}^t \mathbf{e}^{(0)}. \quad (7)$$

Note that the superscript t without brackets denotes an exponent rather than just indicating the iteration number, which is given in brackets.

Using, e.g., the L_2 vector and matrix norms, one can show that the error is bound by

$$\|\mathbf{e}^{(t)}\|_2 \leq \|\mathbf{R}\|_2^t \|\mathbf{e}^{(0)}\|_2.$$

The method will converge for $\lim_{t \rightarrow \infty} \mathbf{R}^t = \mathbf{0}$, which is the case if and only if the spectral radius of the matrix

$$\rho(\mathbf{R}) := \max_{1 \leq k \leq m-1} |\lambda_k(\mathbf{R})| < 1,$$

that is, if the largest eigenvalue of the iteration matrix is smaller than 1. The eigenvalues of the Jacobi iteration matrix \mathbf{R} and weighted Jacobi method \mathbf{R}_ω are given by [34]

$$\lambda_k(\mathbf{R}) = 1 - 2 \sin^2\left(\frac{k\pi}{2m}\right),$$

$$\lambda_k(\mathbf{R}_\omega) = 1 - 2\omega \sin^2\left(\frac{k\pi}{2m}\right),$$

for $1 \leq k \leq m-1$, and the k corresponding eigenvectors can be given by their j -th components [35]

$$w_{k,j} = \sin\left(\frac{jk\pi}{m}\right), \quad 1 \leq k \leq m-1, \quad 0 \leq j \leq m.$$

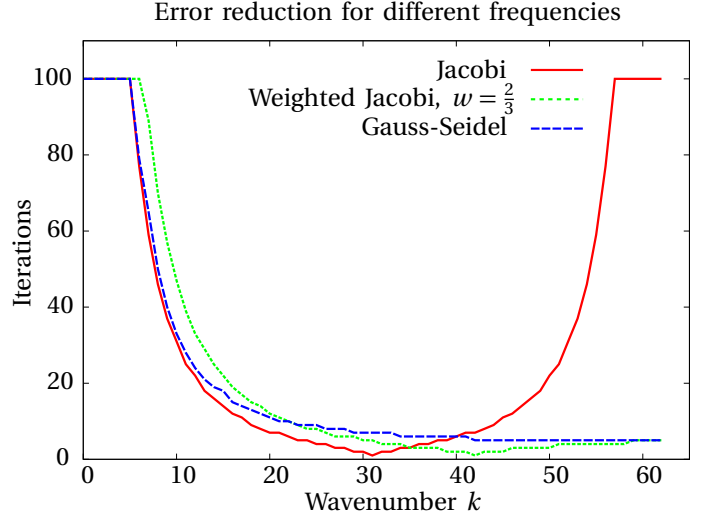


Figure 2: Initial guesses, corresponding to the initial errors, are functions of different frequencies (given by wave number k). Plotted is the number of iterations required to reduce the error by a factor of at least 100 for a model problem with $m = 64$. For the weighted Jacobi and Gauss-Seidel method, high frequencies ($k \geq \frac{m}{2}$) are reduced rapidly, while low frequencies need a considerably larger number of iterations to be reduced by the same factor. Adapted from [34].

The eigenvectors therefore simply correspond to different frequencies (or modes), depending on the so-called wave number k , which indicates the number of half-sine waves the eigenvectors consist of over the $m+1$ subintervals.

The error of our model problem can be expressed as weighted linear combination of these eigenvectors,

$$\mathbf{e}^{(0)} = \sum_{k=1}^{m-1} c_k \mathbf{w}_k,$$

with weights $c_k \in \mathbb{R}$, and using Eq. 7, it can be rearranged to see that after t iterations, the error is given by

$$\mathbf{e}^{(t)} = \sum_{k=1}^{m-1} c_k (\lambda_k)^t \mathbf{w}_k.$$

The frequency component in the error given by \mathbf{w}_k is therefore reduced by a factor of $(\lambda_k)^t$ after t iterations, and the smaller the eigenvalue, the faster this process is. Of interest here is especially the weighted Jacobi method. The proper choice of weight ω guarantees optimal convergence, and it can be shown that the ideal weight for that purpose is $\omega = \frac{2}{3}$ [34]. Then, about half of the eigenvalues – those corresponding to the high-frequency wave numbers $k \geq \frac{m}{2}$ – are of low magnitude. These high frequencies are therefore reduced rapidly, while lower frequencies are damped slowly, cmp. also Fig. 2.

3) *1-D Gauss-Seidel Method*: The Gauss-Seidel method differs from the Jacobi scheme outlined above in Eq. 5 such that it uses the already updated function value $f_{i-1}^{(t)}$ instead of $f_{i-1}^{(t-1)}$. The resulting method is called Gauss-Seidel

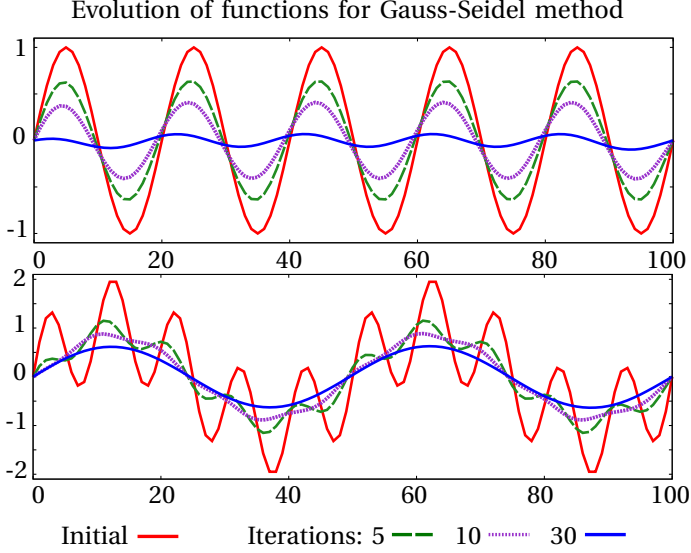


Figure 3: Evolution of functions when applying the Gauss-Seidel method on the 1-D model problem. Initial guesses consisted of functions of different frequencies corresponding to wave number $k = 10$ (top row) and superimposed frequencies with wave number $k_1 = 4, k_2 = 20$ (bottom row). The evolution of the functions is shown for iterations 5, 10 and 30.

method, and the update scheme is modified accordingly to

$$f_i^{(t)} = \frac{1}{2} (f_{i-1}^{(t)} + f_{i+1}^{(t-1)}), \quad (8)$$

and in matrix notation

$$\mathbf{f}^{(t)} = \underbrace{(\mathbf{D} - \mathbf{L})^{-1}}_{\mathbf{R}_G} \mathbf{U} \mathbf{f}^{(t-1)}.$$

As outlined in [35], the eigenvalues and eigenvectors change to

$$\lambda_k(R_G) = \cos^2\left(\frac{k\pi}{m}\right), \quad 1 \leq k \leq m-1$$

and

$$w_{k,j} = [\lambda_k(R_G)]^{\frac{j}{2}} \sin\left(\frac{jk\pi}{m}\right) = \left[\cos\left(\frac{k\pi}{m}\right)\right]^j \sin\left(\frac{jk\pi}{m}\right).$$

Although different frequencies are mixed here, the general property that smooth modes are damped slowly, while the high-frequency modes are eliminated rapidly remains unchanged for the Gauss-Seidel method [34]. This is also demonstrated in Fig. 2, where the Jacobi, weighted Jacobi (for the optimal weight $w = \frac{2}{3}$) and the Gauss-Seidel method were applied to functions of different frequencies, defined by wave number k . Shown is the number of iterations that are needed to reduce the error by a factor of at least 100.

C. Reformulation of Gauss-Seidel for Image Stacks

First, it is important to note again that – unlike assumed for the model problem 2 – it is *not* our goal to minimize

the curvature such that $f''(x) = 0$. This would correspond to eliminating *any* curvature of structures in our anatomical volume. Instead, we merely use the property of Gauss-Seidel to degrade high-frequency variances very fast while mostly preserving low frequencies to our advantage. Furthermore, applying the Gauss-Seidel method on image sequences requires some adjustments of the operations and the notation. A side-by-side view comparing the operations used for the 1-D model problem and as used in the context of image sequences is depicted in Fig. 4.

1) *Transfer of properties and operations to image sequences:* The discrete function values f_i are from now on replaced by the histological images I_i . As stated above, minimizing the curvature now means that the high-frequency disturbances perpendicular to the slice planes should be eliminated, while preserving the lower frequency progression of the anatomical structures along the stack. More important, however, is that the difference or offset $d_{i,j}$ between function values – which in the 1-D case could easily be calculated by subtraction of neighboring function values – has to be defined for images. This requires more in-depth discussion, as the application of the subtraction operator to digital images imposes certain constraints.

The offset $d_{i,j}$ modifies a function value f_j such that it is most similar (or equal) to another function value f_i . For our histology images, this offset is defined as the deformation field $\mathbf{u}(x, y) = \mathbf{u}(\mathbf{x})$ as defined in section II-A, relocating the pixels of one image I_j such that it is most similar to another image I_i , $I_i = I_j(\mathbf{x} - \mathbf{u}(\mathbf{x})) =: I_j \circ \mathbf{u}$. In contrast to the 1-D real case, however, where correcting a function value by the offset lets it assume an exactly calculated value, a real image transformed by a deformation field will never exactly look like the image it was registered to. This is because the deformation is restricted such that it mimics the deformations that are imposed on the tissue slices during cutting.

2) *Iteration scheme:* To express the Gauss-Seidel iterative update scheme in Eq. 8 such that it can be transferred to images and deformation fields, we expand and reformulate it,

$$\begin{aligned} f_i^{(t)} &= \frac{1}{2} (f_{i-1}^{(t)} + f_{i+1}^{(t-1)}) \\ &= \frac{1}{2} (f_{i-1}^{(t)} + f_{i-1}^{(t)} - f_{i-1}^{(t)} + f_{i+1}^{(t-1)}) \\ &= \frac{1}{2} \left(f_{i-1}^{(t)} + f_{i-1}^{(t)} + \underbrace{(f_{i+1}^{(t-1)} - f_{i-1}^{(t)})}_{:=d_{i-1,i+1}} \right) \\ &= \frac{1}{2} (2 \cdot f_{i-1}^{(t)} + d_{i-1,i+1}) \\ &= f_{i-1}^{(t)} + \frac{1}{2} d_{i-1,i+1}, \end{aligned} \quad (9)$$

where $d_{i,j}$ denotes the difference between the current best approximations of the function values f_i and f_j , which in \mathbb{R}^1 corresponds to a simple subtraction $d_{i,j} = f_j - f_i$.

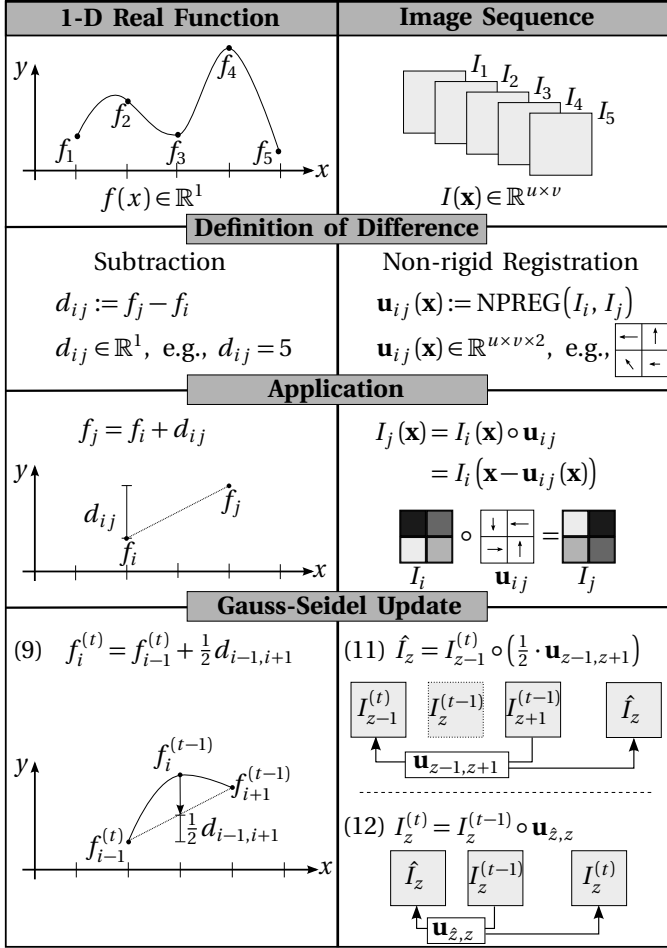


Figure 4: Comparison of corresponding components and operations for 1-D model problem (left column) and image sequence (right column) when the Gauss-Seidel method is applied. Row 1, Input: in case of the model problem a sequence of discretized function values $f_i \in \mathbb{R}^1$, and in our case an image sequence $I_i \in \mathbb{R}^{u \times v}$. Row 2, difference d_{ij} between two input elements: calculated by subtraction in the model problem. For images, the element transforming one image into the other image – corresponding to the difference – is given by the deformation field \mathbf{u}_{ij} calculated using non-rigid registration. Row 3, application of difference d_{ij} : by simple addition in $f_i \in \mathbb{R}^1$, while a deformation field to transform image I_i to image I_j is applied via resampling. Row 4, Gauss-Seidel update: for the model problem achieved by relocating the current value to the midpoint between its neighbors (by adding half the difference between these neighbors). In our case, an image is updated by transforming it into the mean shape of its neighbors, which first requires the creation of an interpolated intermediate image \hat{I}_z .

The current function value $f_i^{(t)}$ is given by the previous function value, plus half the distance from that to the following function value, i.e., simple linear interpolation.

Equation (9) basically says that the new updated value is given by the preceding value, plus half the difference

between the preceding and succeeding value. In terms of images and deformation fields, this update is equivalent to changing an image by half the deformation transforming the preceding image to the succeeding image, please refer also to Fig. 4.

Therefore, the Gauss-Seidel update formula as applied to images is given by

$$I_z^{(t)} = I_{z-1}^{(t)} \circ \left(\frac{1}{2} \cdot \mathbf{u}_{z-1,z+1}\right) \quad (10)$$

Here, $I_z(x, y) =: I_z$ is the digital image at position z of the image sequence. As detailed above, the difference $\mathbf{u}_{z-1,z+1}(x, y) =: \mathbf{u}_{z-1,z+1}$ – effectively the corresponding concept to the difference $d_{i,j}$ of the model problem – is defined as the deformation field that transforms image $I_{z+1}^{(t-1)}$ into image $I_{z-1}^{(t)}$, and is obtained using non-rigid registration between these two images. Unfortunately this would discard any tissue information that was originally contained in slice I_z which is currently updated. Therefore another adjustment has to be made to ensure that all anatomical information that is contained in the slice images is used for reconstruction. The t -th approximation of image I_z is not given by merely deforming the previous image, as indicated in Eq. (10), but instead this approximation is used as interpolated intermediate image $\hat{I}_z^{(t)}$, as described in [36]. This intermediate image is then used as reference, to which the original histology image is non-rigidly registered. In this way, the anatomy contained in the original slice image I_z is preserved, but deformed to match the interpolated image calculated by Gauss-Seidel iteration in Eq. (10).

The iteration scheme is therefore modified to

$$\hat{I}_z = I_{z-1}^{(t)} \circ \left(\frac{1}{2} \cdot \mathbf{u}_{z-1,z+1}\right) \quad (11)$$

with $\hat{I}_z^{(t)}$ indicating the artificial, interpolated image using the neighboring images of the t -th iteration, and the actual new image at position z is given by

$$I_z^{(t)} = I_z^{(t-1)} \circ \mathbf{u}_{z,z} \quad (12)$$

where $\mathbf{u}_{z,z}$ is the deformation field between the original image at position z of iteration $t-1$ and the interpolated image \hat{I}_z .

3) *Boundary conditions*: In general, boundary conditions specify the values or the behavior of the solution to a (partial) differential equation at the boundaries of the domain. Two of the most commonly used types of boundary conditions are Dirichlet boundary conditions, which define specific function values of the solution at the boundary, or Neumann boundary conditions, imposing constraints on the derivative of the function at the boundary. In both cases, these values or derivatives are known in advance.

In our case, the function values at the boundary of our domain, i.e., the *corrected and unwarped* images at the beginning and the end of the image stack, are unknown. As we do not use any prior information via reference volumes, we also cannot reliably assume any specific behavior of

the ‘‘anatomic function’’ at these positions. In addition, the images at the boundaries of the image stack also have to be unwarped during the optimization routine.

To achieve this, our domain is enlarged at both ends by one image respectively. Which kind of image is used depends on the boundary condition one wants to assume.

Dirichlet boundary conditions correspond to copying one image - e.g., the original histological image prior to unwarping - as fixed boundary value. This works well if it is known that the images at the borders do not show strong deformations. After t iterations, the problem domain then consists of the updated images and the original boundary images as boundary conditions, $\Omega^{(t)} := (I_1^{(0)} := I_0^{(t)}, I_1^{(t)}, I_2^{(t)}, \dots, I_Z^{(t)}, I_{Z+1}^{(0)} := I_Z^{(t)})$. However, a mostly artifact-free image can generally not be guaranteed, and in extreme cases such an outlier could adversely affect a significant portion at the end of the stack.

To at least dampen the effect of such a possible outlier slice, we choose to use Neumann boundary conditions. Here, the derivative of the function is set to zero. This is achieved by copying the last updated version of the boundary images of the image stack as new boundary condition images after each iteration of the optimization routine. After t iterations, the problem domain is then given by $\Omega^{(t)} := (I_1^{(t)} := I_0^{(t)}, I_1^{(t)}, I_2^{(t)}, \dots, I_Z^{(t)}, I_{Z+1}^{(t)} := I_Z^{(t)})$.

4) *Convergence*: Regarding the convergence, note that the theoretical convergence behavior in practice is affected by the regularization of the deformation within the slice plane x-y and the severity of the deformations. Convergence will therefore be slower than what theory predicts. In addition, the assumption of uniform subintervals - equivalent to equally spaced histology slices - might not be fulfilled, since tissue slices often get lost or are severely disrupted such that they are not suitable to be used for reconstruction. Just removing such an image from the stack is not an option, since this would compress the anatomy at this position. Instead, we use interpolation of slices as outlined in [36] to fill the gap. This restores the uniformity of the subintervals, and therefore the convergence requirements outlined above.

5) *Algorithm*: To prevent repeated propagation of possible defects in the slices along the stack, the Gauss-Seidel scheme is iteratively applied to the stack, with alternating directions (also known as symmetric Gauss-Seidel method). This also effectively reduces any bias effect that non-rigid registration methods often show when they are applied, depending on the direction along the stack. After a first update of the entire stack, including the boundary condition images, the scheme is repeated in reverse order, starting with the images that were updated last in the previous iteration. The algorithm for our proposed image unwarping strategy is depicted in Algorithm 1. To prevent artifacts from repeated interpolation during the update step, we accumulate all calculated update deformation fields for a specific image I_j into one deformation field $\mathbf{u}_{j,accu}^{(t)} = \mathbf{u}_j^{(t-1)} \circ \dots \circ \mathbf{u}_j^{(0)}$, which is finally applied to the original image $I_j^{(0)}$ to generate the image $I_j^{(t)}$ after t

Algorithm 1 Proposed method for image unwarping using a Gauss-Seidel iteration scheme and Neumann boundary conditions.

```

Input
   $I_1^{(0)}, \dots, I_Z^{(0)}$  histological image sequence
   $N$  number of iterations
Expand image domain by Neumann b.c.
   $I_0^{(0)} \leftarrow I_1^{(0)}, I_{Z+1}^{(0)} \leftarrow I_Z^{(0)}$ 
for iteration  $t=1, \dots, N$ 
  for image  $j=1, \dots, Z$ 
     $\mathbf{u}_{j-1, j+1} = \text{NPREG}(I_{j-1}^{(t)}, I_{j+1}^{(t-1)})$ 
     $\hat{I}_j = I_{j+1}^{(t-1)} \circ (\frac{1}{2} \cdot \mathbf{u}_{j-1, j+1})$ 
     $\mathbf{u}^* = \text{NPREG}(\hat{I}_j, I_j^{(t-1)})$ 
     $\mathbf{u}_{j, accu}^{(t)} = \mathbf{u}_{j, accu}^{(t-1)} \circ \mathbf{u}^*$ 
     $I_j^{(t)} = I_j^{(0)} \circ \mathbf{u}_{j, accu}^{(t)}$  update
  end
   $I_0^{(t)} \leftarrow I_1^{(t)}, I_{Z+1}^{(t)} \leftarrow I_Z^{(t)}$ 
  reverse sequence  $(I_0^{(t)}, I_1^{(t)}, \dots, I_Z^{(t)}, I_{Z+1}^{(t)})$ 
end
Output
   $I_1^{(N)}, \dots, I_Z^{(N)}$  unwarped image sequence

```

iterations. As was already mentioned before, this algorithm can be used with other registration methods tailored to the reconstruction problem at hand. Note however that our algorithm requires the scaling and composition of calculated slice transforms. If the chosen registration method does not directly offer this possibility, we propose to create a dense deformation field from the calculated slice transformation, which should be possible regardless of the choice of deformation model.

III. EVALUATION AND RESULTS

To evaluate the performance of our reconstruction method, it is tested on synthetic and real data sets. Each of the experiments was designed to evaluate a different characteristic of our method.

The applicability of the Gauss-Seidel method in the context of images and deformation fields, and the convergence and smoothing properties for different frequencies is demonstrated using synthetic slice data sets. The second experiment uses a CT slice sequence that was non-rigidly transformed to quantify the error reduction over the number of iterations for more complex data for which the ground truth is known. Finally, we show the quality of our reconstructions using a real histology data set. We compared our results to atlas and MR images, and reconstruction results by [2], who provide their reconstructions online.

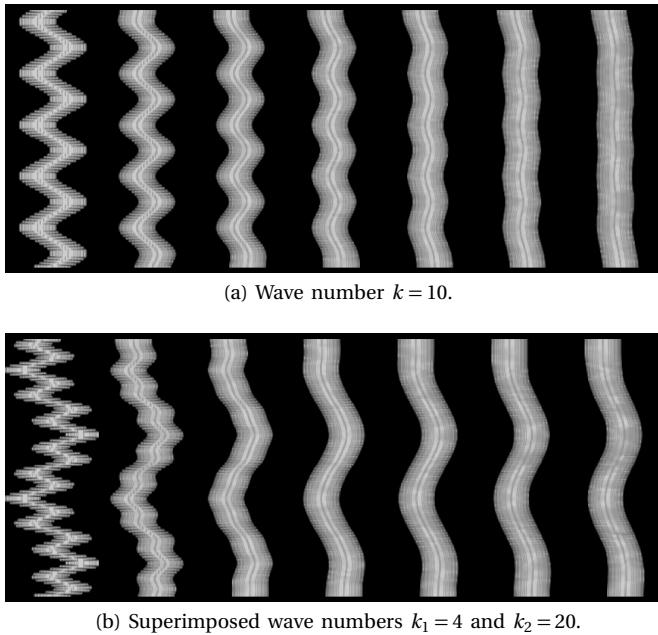


Figure 5: Volume renderings of data sets with different frequencies, defined by the wave number k , evolving over time. Shown are the original data sets, and after 5, 10, 15, 20, 25 and 30 iterations. Note the similarity of the results to the results shown for the 1-D model problem (fig. 3).

A. Synthetic Data

Every data set consists of $n = 100$ images of size 121×121 . A white circle with a diameter of 21 pixels is placed on black background. The circle center changes its position along the image sequence according to a sinusoidal function. Starting at the first image with center (x_c, y_c) , the coordinates of the circle center with coordinates (x_{cc}, y_{cc}) on slice z is given by

$$(x_{cc}, y_{cc})_z = (x_c, y_c) - a \cdot \sin\left(\frac{zk\pi}{n}\right).$$

Here, a denotes the amplitude of the sinusoid, and was chosen as $a = 10$. k denotes the wave number of the desired frequency, which corresponds to k half sine waves along the entire slice sequence. This emulates a smoothly varying anatomical structure. Several data sets were prepared in this manner, with frequencies $k = \{4, 10, 20, 40, 60, 80, 90\}$. In addition, data sets with two superimposed frequencies - one low frequency of $k_1 = 4$ and a high frequency with $k_2 = 20$ resp. $k_2 = 40$ were generated using

$$(x_{cc}, y_{cc})_z = (x_c, y_c) - a \cdot \left[\sin\left(\frac{zk_1\pi}{n}\right) + \sin\left(\frac{zk_2\pi}{n}\right) \right].$$

To measure the effect of the Gauss-Seidel registration scheme on the different frequency components in the slice volumes, the mean squared error (MSE) between the respective volumes and a reference volume consisting of a centered cylinder is calculated. As the largest part of the convergence happens during the first iterations, the MSE was calculated for each of the first 10 iterations, and every

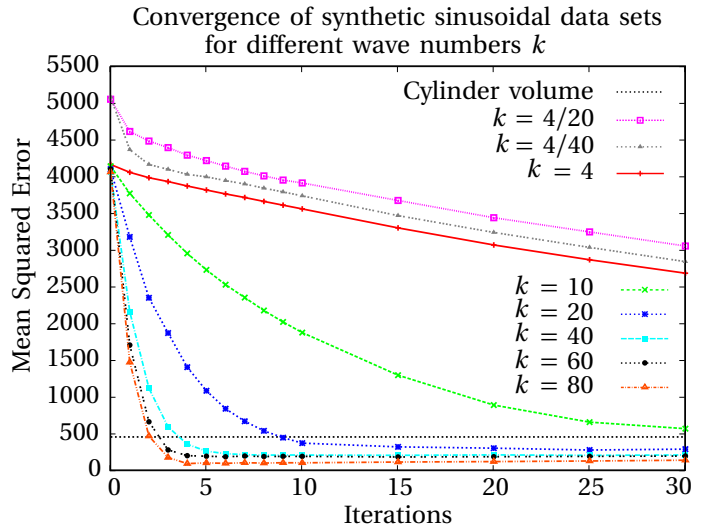


Figure 6: Reduction of MSE for volumes of different frequencies. The horizontal dashed line represents the MSE between the cylindrical volume and a rigidly registered version of itself that was shifted by 2.5 pixels in x and y .

5th after that, for a total of 30 iterations. You can see the differences in convergence for volumes with different wave numbers in fig. 6. To help interpret the magnitude of the MSE values, the MSE between the original volume and a rigidly registered shifted version of the original volume (by 2.5 pixels in x and y) is plotted as horizontal line.

Figure 5 visually shows volume renderings after several iterations for two different data sets. The first one was created with a moderate wave number $k = 10$. The frequency is gradually decreased, and still slightly visible after 30 iterations. The second data shows two superimposed frequencies with wave numbers $k_1 = 4$ and $k_2 = 20$. Here, the high frequency component is eliminated after about 15 iterations, while the low-frequency component is mostly preserved even after 30 iterations. The slightly flattened appearance at the upper and lower ends of this data set is an effect of the boundary condition, which kind of propagates the zero derivative condition into the data set. However, this experiment quantitatively as well as visually confirms the theory that the low frequencies are mostly preserved, while the high frequencies are efficiently eliminated, even when frequencies are superimposed. In addition, we could show that the Gauss-Seidel method is applicable in the domain of images and deformation fields, while featuring the same smoothing properties as for real functions.

To justify our decision to use the Gauss-Seidel method, we repeated the experiment on three data sets representing low ($k = 4/20$), medium ($k = 10$) and high frequency ($k = 80$) functions using the Jacobi method instead of Gauss-Seidel. Here, the calculation of the interpolated intermediate slice \hat{I}_z in Eq. 11 depends not on the already updated slice $I_{z-1}^{(t)}$, but on the previous iteration $t-1$, $I_{z-1}^{(t-1)}$. Beside this difference, all other parts of the algorithm were identical to our experiment using the Gauss-Seidel

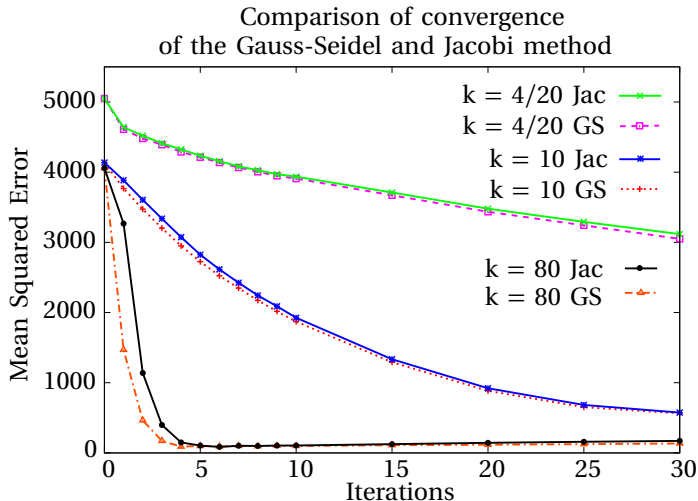


Figure 7: Reduction of MSE for selected volumes, reconstructed using the Gauss-Seidel method (GS) and the Jacobi method (Jac).

method.

Figure 7 shows a comparison of the convergence using both methods. Especially for the high-frequency data set $k = 80$, the Gauss-Seidel method converges significantly faster than the Jacobi method in the first iterations, just as theory predicts, cmp. Fig. 2. For all experiments, the MSE values using the Gauss-Seidel method are lower than the MSE values using the Jacobi method. However, the difference between both methods in the later iterations is not very substantial, being about 2%. Since our goal is to eliminate the high-frequency errors as fast as possible, using the Gauss-Seidel method is a natural choice, and was therefore exclusively used for the other experiments. If for some reasons the Jacobi method is used, e.g., due to simpler parallelization of the method, which will be discussed in section III-E – the resulting reconstructions will show a similar quality as those created using the Gauss-Seidel method.

B. Synthetic Histology Data

To show the efficacy of our approach on more complex data, we generated a synthetic histological slice sequence using a CT data set of an armadillo [37]. A subset of 100 CT images, cropped and resized to 464×387 pixels, were individually transformed with non-rigid transforms. As other artifacts typical for digital histology images are not present, the reconstruction quality independently of the preprocessing methods - including the quality of the linear alignment prior to unwarping - can be evaluated.

The deformations for each image were synthesized using B-Splines with random offsets at the B-Spline grid points. The maximum dislocation at a grid point was restricted to ± 10 pixels, which was empirically chosen to yield deformations that were visually similar to real histological images. Two experiments were implemented. First, ten different versions of the deformed CT data set were created

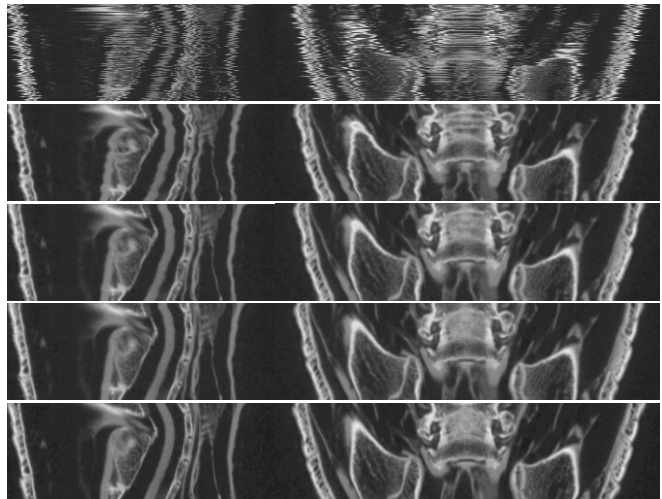


Figure 8: Synthetic CT data set with biased deformations. Rows 1-4: Deformed data set, and after 5, 10 and 15 iterations. Bottom row: Original CT data.

using the mentioned method (these volumes will be called unbiased volumes).

Second, the process generating the random deformations was adapted to emphasize offsets in one direction. This corresponds more to real histology data, which is more likely deformed along the cutting direction. Again, ten different volumes were generated, which will be denoted biased volumes. The first experiment thus enables to quantify the error stemming from the reconstruction algorithm independently from a deformation bias. The second experiment then demonstrates the effect of the bias on the reconstruction result.

Qualitatively, as can be seen in Figure 8, the deformations are immensely reduced after 5 iterations, and after 15 iterations there are barely differences to the original CT data set visible.

Since the ground truth deformation is known in this experiment, the Target Registration Error (TRE) as defined by Fitzpatrick et al. [38] was calculated after each iteration. The TRE denotes the difference between the true location of a pixel before it was dislocated using the generated deformations, and the location of that pixel after our unwarping strategy was applied, which ideally should be zero. In case of the datasets that were deformed by a biased random deformation, the bias leads to the anatomy being shifted in a certain direction on average. As this global shift is not relevant for the reconstruction, we have to subtract the global mean shift $\mu_{\mathbf{u}_{\text{true}}}$ from the ground truth deformation. In addition we ignore pixels belonging to the background (air, pixels outside the volume and field of view). The background values are determined by simple thresholding. The resulting mask $M(x,y)$ which is 0 for all background pixels and 1 otherwise is used together with the mean shift to calculate the TRE as

$$\text{TRE} = \frac{1}{n} \sum_{x,y,z} M(x,y) \cdot (\mathbf{u}_{z,\text{true}}(x,y) - \mu_{\mathbf{u}_{\text{true}}} - \mathbf{u}_{z,\text{calc}}(x,y))^2$$

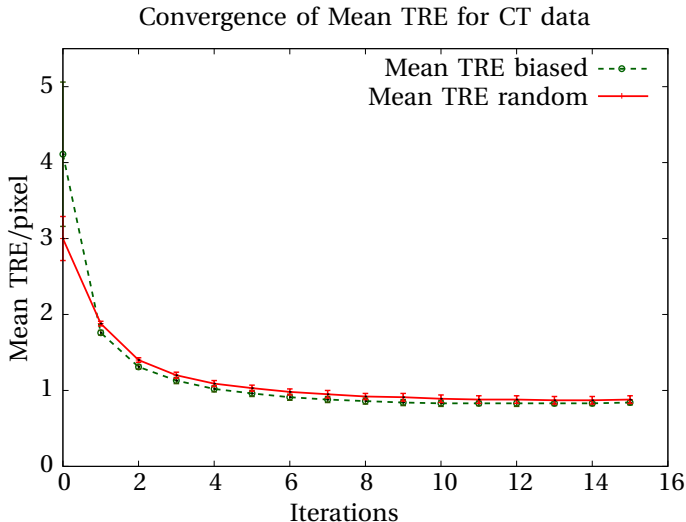


Figure 9: Mean and standard deviation of the Target Registration Error TRE, calculated for the two sets of deformed CT data sets. For more details, please refer to the text.

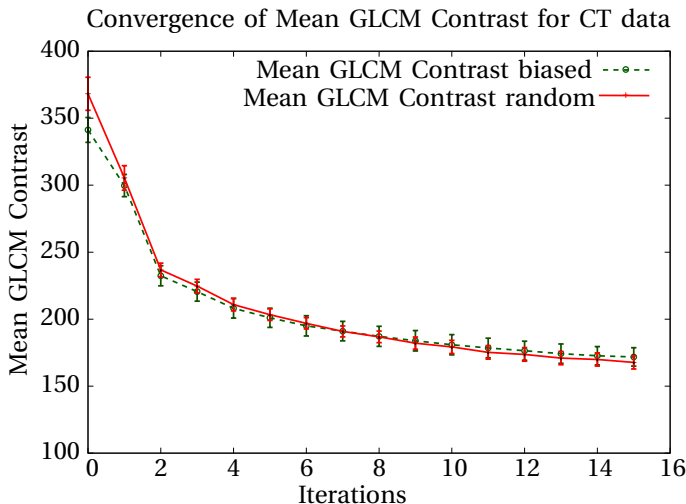


Figure 10: Mean and standard deviation of the GLCM contrast feature, calculated for the two sets of deformed CT data sets.

where n denotes the number of pixels in the volume, $\mathbf{u}_{z,\text{true}}$ and $\mathbf{u}_{z,\text{calc}}$ denote the ground truth deformation and calculated deformation of slice image z respectively, and $M(x, y)$ is a binary mask image with an entry 1 if there is anatomy at the corresponding location and 0 otherwise. In this way, we get the mean offset from the ground truth location per pixel for a given volume.

Figure 9 shows the mean and standard deviation of the Target Registration Error, calculated for the two experiments. The TRE converges very fast to an average offset of about 1 pixel. The reduction in the TRE shows that at least for the deformed CT data sets our method is able to reverse a high amount of the actual deformations in the data sets.

Since the ground truth deformation of histology data sets is usually not known, we additionally quantify the

achieved smoothness of the reconstructed volume. To do this, one inevitably has to compare neighboring pixels and evaluate their similarity. Therefore in theory, every similarity measure used in image registration can be used for this purpose (examples of measures used for this purpose are cross-correlation [39] and Sum of Squared Distance [21]). Due to their similarity to the optimization criterion in our non-rigid registration objective function, these measures are inappropriate for evaluation purposes. Another popular measure is the Correspondence Alignment Measure (CAM,[40], [26]), which assumes that in an ideal reconstruction, a specific point lies exactly at the midpoint between its two neighbors. However, this is also basically what we optimize via the Gauss-Seidel Measure and additionally requires the correct identification of corresponding points. Last, the calculation of overlap was used before, e.g., in [39], which requires the segmentation of the structures of interest

Instead, we choose the contrast feature calculated from the gray-level co-occurrence matrices (GLCMs) as introduced by Haralick et al. [41] to quantify the achieved smoothness of the reconstructions, similar to [39] and [13]. Thereby we are independent from correspondence search and segmentation issues, and avoid a measure too similar to our optimization criterion.

The GLCM contrast feature measures the amount of contrast in an image by investigating the frequency of certain intensity pairings of neighboring pixels. Before reconstruction, neighboring pixels in axial direction (along the stack) more likely show high intensity differences – that is, higher contrast – as opposed to after reconstruction (cmp. top row and bottom row of Figure 8). Decreasing contrast therefore corresponds to a better match of neighboring slices, and consequently to smoother morphological structures along the stack.

For a given volume, we add up the values calculated for each volume slice extracted in axial direction. Figure 10 shows the decrease of the contrast GLCM measure over the iterations. It shows that our unwarping strategy effectively restores anatomical smoothness for the volume, mostly over the first few iterations.

As we have already stated in the introduction, a smooth reconstruction does not guarantee an anatomically correct reconstruction. Curved structures might be effectively straightened by the reconstruction method, leading to extremely good smoothness values, while at the same time introducing strong unnatural deformations to the anatomy. However, our experiments show a strong correlation of the GLCM measure with the TRE. The fact that our method is able to approximate the true deformations of the slices confirms the intuition that using our method, smoother looking data sets are indeed closer to the real anatomy.

C. Histology Data

Finally, we applied our method to a Nissl-stained data set of a mouse brain, available online from Ju et al. [2]. The

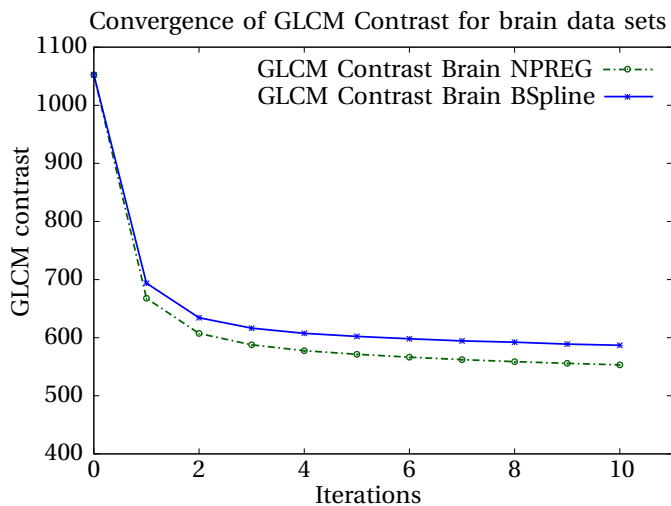


Figure 11: Convergence of the GLCM contrast feature calculated for the successive versions of the image stack over the iterations, for two different deformation models.

data set consists of 350 coronal, cryo-sectioned and Nissl-stained histological images with a resolution of 850×670 pixels, $25 \mu\text{m}$ slice thickness and $15 \mu\text{m}$ per pixel.

Ju et al. provide an unaligned, original data set without intensity normalization but homogeneous illumination, as well as a rigidly registered and normalized version of the data, and their reconstruction result.

As this article deals with the reversal of the local deformations of the slices, we applied our method to the aligned and intensity-normalized data set. The normalization of the slice intensities also enabled us to employ the sum-of-squared differences (SSD) measure in our experiment. It is faster to calculate than, e.g., the multimodal measure Mutual Information (MI), which would normally be appropriate in cases with inter-slice intensity differences. Experiments using the MI delivered similar results, while taking more computation time. Optimal values for the weighting factor of the regularizer were empirically chosen, as was the number of 10 iterations for our method.

To show that our initial statement – that our method works independently from the chosen non-rigid registration method – is valid, we performed a second reconstruction of the mouse brain data set. Instead of our presented non-parametric, non-rigid registration method, we used a registration method using a parametric B-Spline based deformation model as proposed by Rueckert et al. [42] and implemented in the Insight Toolkit [43].

Figure 11 shows the convergence of the GLCM contrast feature values, calculated for successive versions of the image stack over the iterations for both experimental setups.

In both cases, the contrast values decrease significantly in the first iterations, indicating an increase in contour smoothness. The slightly slower convergence of the B-Spline-based registration can be attributed to the less flexible deformation in this specific setup as compared to our non-parametric approach.

To compare our result with other state-of-the-art imaging modalities, we created virtual slices through the reconstructed volume. Figure 12 shows a direct comparison of virtual sections to an atlas image from Paxino’s Atlas [44], and Fig. 13 to a T1-weighted MR volume from the Waxholm space [1].

Furthermore, we compared our reconstruction result to Ju’s reconstruction, which is also provided online. As you can see in Figure 14, the brain structures in general appear more clearly, and boundaries are significantly smoother in our reconstruction. In addition, the fiber-like structures that are barely visible on the left are clearly visible with our method, but are also visible in the MR volume 13. This is most likely due to the calculation of the deformation on the bilaterally filtered images, which in this case prevents matching of the connected structures. For comparison, the corresponding slices extracted from the rigidly aligned input stack are shown in the top row. Even more profound is the comparison of the original and warped coronal sections, cmp. Figure 15. The warp filtering approach clearly introduces unnatural deformations to the slice, whereas the unwarp slice using our approach appears unaffected by artificial deformations.

1) *Effect of slice defects on reconstruction result:* As mentioned already, due to the severe mechanical stress that is imposed on the tissue during slice preparation and staining – e.g., cutting, relocation, heating, etc. – and depending on the robustness of the tissue that is processed, the final slice images can show different artifacts, which inevitably have an influence on the reconstruction result.

How severe the effect of the defects on the reconstruction result is depends on the size of the defect, and the regularization of the allowed deformation in the non-rigid registration method. Smaller defects, e.g., small tears or the bubble-like defects visible in the brain data set, do not show significant effects in our experiments. The reason is usually that the change in the calculated deformation field due to the defect is so local that the regularization term – which emphasizes smooth non-local deformations – prevents said deformation.

If the defect is large (e.g., large parts missing from the slice, or larger folds), the corresponding image parts have enough weight in the similarity measure part of the non-rigid registration objective function so that unwanted deformations are introduced as far as the regularizer allows them. Such a defect should therefore always be treated before reconstruction. Strategies for this include eliminating the slice if the loss of anatomical information is tolerable, repairing by complete or partial interpolation of the defect slice, cmp. [45],[36],[27], or by using artifact-tolerant non-rigid registration methods [46], [47]. For medium-sized defects, masking the defect image parts in the registration might also be sufficient to achieve a satisfactory result.

If such a large defect is overlooked, however, the resulting unwanted deformations will be propagated along the stack, spreading to the left and right of the original defect slice, an effect demonstrated in Figure 16.

We performed an experiment illustrating this effect.

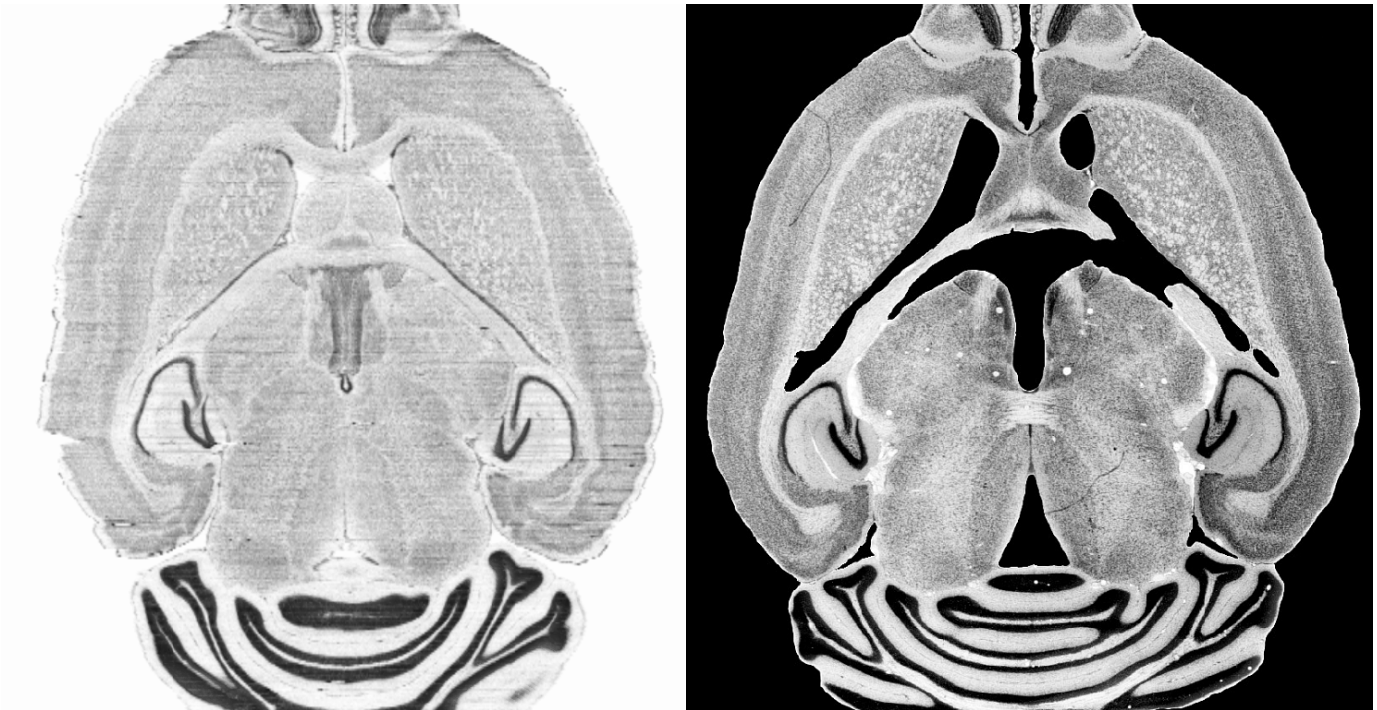


Figure 12: Left: Virtual section through the reconstructed volume. Right: Real histology slice from Paxino's Atlas [44]

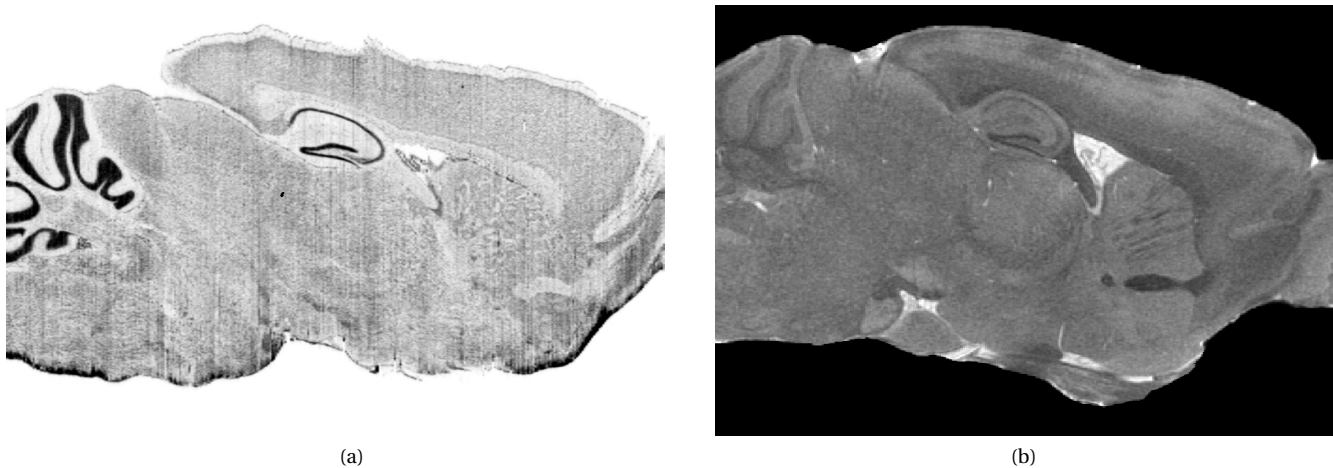


Figure 13: a) Virtual section through the reconstructed volume. b) Sagittal section of a T1-weighted MR volume from the Waxholm space [1].

Here, we manually erased a significant amount of the tissue of slice 30, simulating a larger defect like it might occur in histological slice sequences. When unwarping the volumes once with the corrupt slice, the effect of propagated distortions of the tissue is clearly visible as compared to the original reconstruction, cmp. Figure 16. After 6 iterations, the effect was visible from slices 21 to 39. When replacing the defective slice with an interpolated one [36] before applying our method, the morphology in the reconstructed image stack again seems to be intact, with only small differences to the original reconstruction.

D. Complexity and Convergence

Usually histological image reconstruction is not a time-critical process. The time that is needed for image unwarping mostly depends on the non-rigid registration method that is used, and the image size. The Gauss-Seidel scheme we employ is generally independent from the type of non-rigid registration method that is used, but determines the number of registration operations that are needed. For a data set consisting of K images (excluding the boundary condition images) and using N iterations, the number of non-rigid registrations is given by

$$\#(\text{NPREG}) = 2 \cdot K \cdot N.$$

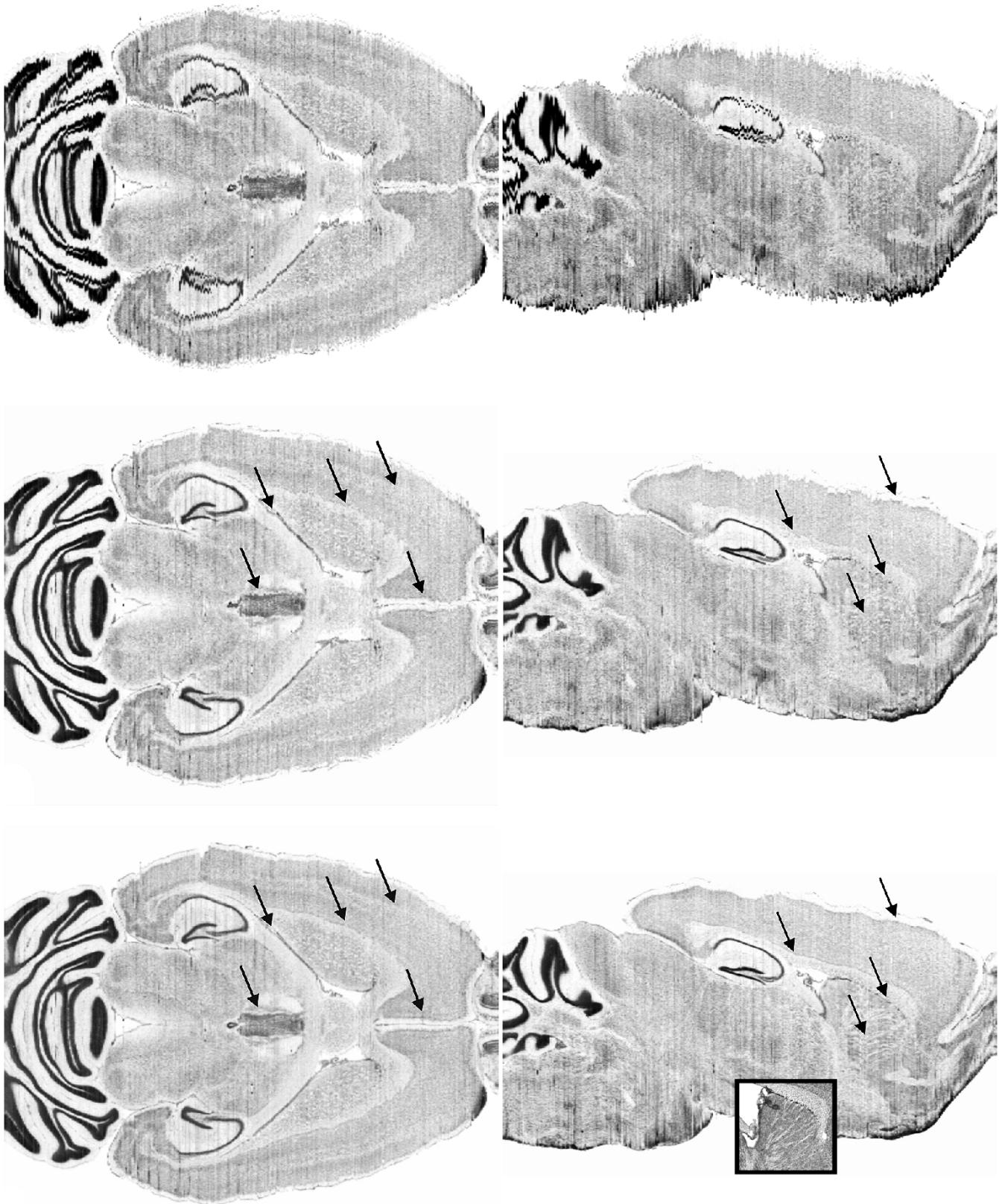


Figure 14: Virtual axial (left) and sagittal (right) sections. Top: After rigid alignment. Middle: Reconstruction from Ju et al. [2]. Bottom: Our approach. Inset: Detail image from Paxino's Atlas (plate 110) [44] showing the fiber bundles in the caudoputamen region.

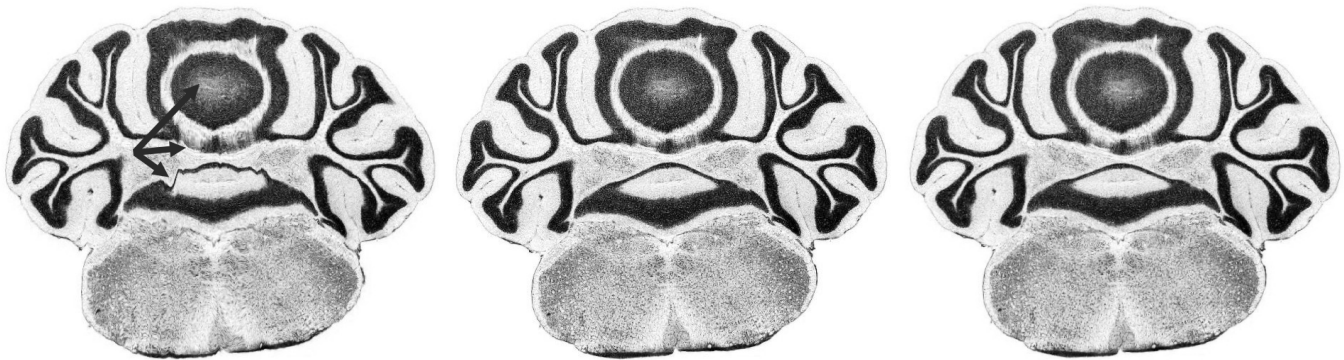


Figure 15: Visualization of the effect of in-plane deformations used for unwarping. Note the middle section of the images. Left: From Ju et al. [2]. Middle: Original histology slice. Right: Our proposed method.

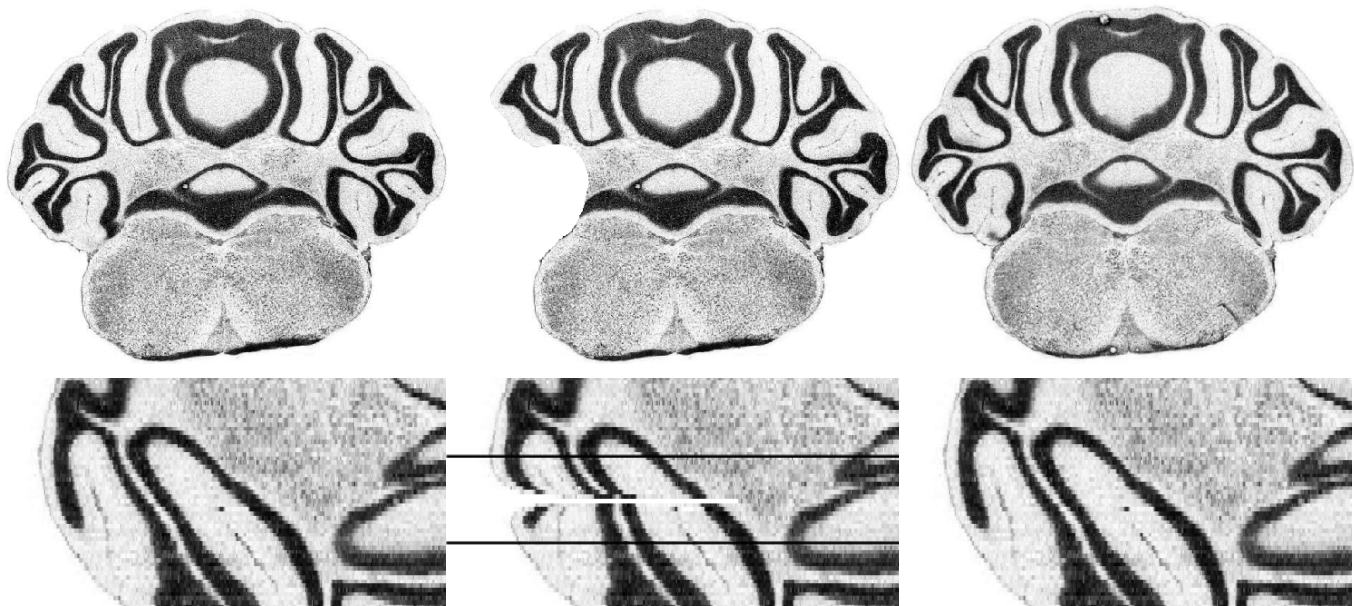


Figure 16: Visualization of the effect larger defects have on the reconstruction result after 6 iterations. Left: Ground truth reconstruction with intact slice 30. Middle: Distorted reconstruction for artificially destroyed slice 30. Lines indicate boundaries of the distorted region. Right: Reconstruction result using an interpolated replacement for slice 30 (top right).

Depending on the data set at hand, this number can get quite large. The reconstruction of the mouse brain data set with its 350 slice images and 10 iterations required in total 7000 registrations. For the image size of 850×670 pixels, one non-rigid registration needed in average 19.7 seconds to finish on a 3.2 GHz workstation with 6 GB RAM. The total time to reverse the deformations of the entire image stack therefore was 38:24:11 hh:m:s. Another advantage of our method is that due to the sequential type of processing, the memory requirements are low, even for very highly resolved histology images.

As with any fixed-point iteration method, the decision of when to stop the iteration process also arises in our method. Here, we propose to investigate the convergence of the method as stopping criterion. A fixed-point iteration method is converged, when the change of the calculated solution from one to the next iteration is smaller than

a – usually empirically chosen – constant. In our case, one could calculate the MSD between successive versions of the image stack over the iterations, cmp., e.g., Figure 17, and falls below a certain limit. Another possibility is, of course, to let an anatomical expert decide when the reconstruction result is satisfactory.

E. Parallelization

Due to the potentially high number of images and therefore registration operations, the parallelization of our method would potentially lead to a significant acceleration of the reconstruction process. Since the update of a value using the Jacobi method depends only on the predecessor and successor of the same iteration number, parallelization is more straight-forward here. One strategy is, e.g., to assign equal parts of the data set to different processors. After updating the images within the blocks, only the

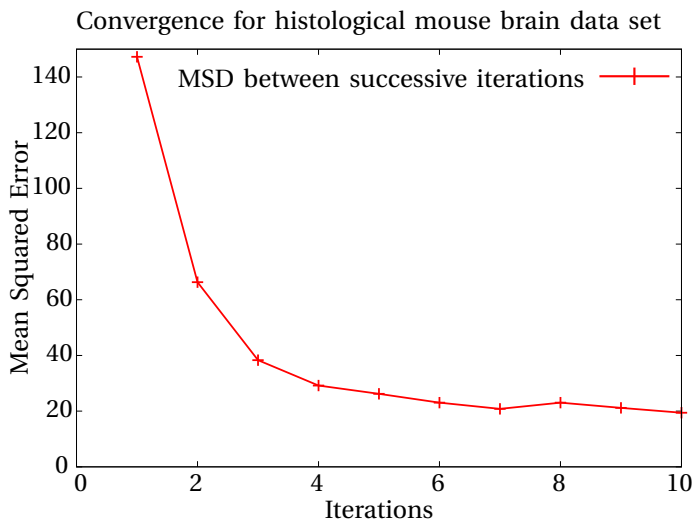


Figure 17: MSD between successive versions of the image stack over the iterations. The first value denotes the MSD between the rigidly registered volume, and the first iteration.

images at the boundaries of the different blocks have to be updated, which can also be done in parallel. Since the update of a value in the classical Gauss-Seidel method uses an already updated predecessor, parallelization is not as obvious. Still, it is possible using a method called Red-Black Gauss-Seidel, in which the data is alternately distributed into two disjoint subsets, red and black. Within each of the subsets, the individual update operations are independent of each other, and can therefore be performed by several processors [34].

IV. SUMMARY

We could show that the iterative Gauss-Seidel method is applicable for image unwarping of histological slice sequences. The methods' property of quickly eliminating high-frequency disturbances and degrading low-frequency components only very slowly is well suited to reverse the deformations due to slice cutting, while preserving the naturally smooth curvature of anatomical structures. The final quality of the reconstruction is comparable to state-of-the-art technologies like atlases and MR devices. Furthermore, as we showed in our experiments, our approach can be applied independently from the non-rigid registration method that is used, and is therefore highly versatile.

In principle, both the Jacobi and Gauss-Seidel methods can be used. While the dampening of high-frequency artifacts is faster for the Gauss-Seidel method during the first iterations, the Jacobi method might offer benefits as it is easier to parallelize than Gauss-Seidel.

However, the reconstruction result strongly depends on the quality of the global alignment. The overall shape of the tissue stack will not be altered much during unwarping, and therefore has to be verified in advance. This is usually achieved using rigid registration. If corrections of

an automatically achieved alignment are required, manual refinement is still an option, which in contrast to that is prohibitive for image unwarping due to the high number of degrees of freedom that would have to be defined manually in this case.

Furthermore, our method assumes that the low-frequency components of the unwanted artificial deformations still have a higher frequency than the high-frequency components of the anatomical deformations. Especially extremely curved structures will be subject to some straightening, although in most cases this effect should not be of high relevance.

There are always at least partly defective images contained in a histological slice sequence. These defects negatively affect the deformation fields calculated for image unwarping, e.g., by "pulling" tissue into regions where the tissue is missing naturally or due to cutting artifacts. This can then be propagated to neighboring images, leading to unnaturally deformed parts in a certain neighborhood around the defect. This might be prevented using repairing or replacement strategies before unwarping.

To conclude, our approach is able to effectively reverse the deformations imposed on histological tissue sections during cutting. Its versatility enables easy adaptation to the specific task at hand. Due to the sequential processing and the possibilities for parallelization, it is also suitable for very highly-resolved histology images and image sequences consisting of a large number of slices. Therefore it offers a valuable contribution for the anatomically sound reconstruction of histological image sequences.

ACKNOWLEDGMENT

We thank Ju et al. for providing the histology data set and their reconstructions online. T1 and T2* data set courtesy of the Duke Center for In Vivo Microscopy, an NIH/NIBIB Biomedical Technology Resource Center (P41 EB015897). We also thank Chimaera GmbH (Erlangen) for providing the registration libraries. The authors gratefully acknowledge funding of the Erlangen Graduate School in Advanced Optical Technologies (SAOT) by the German National Science Foundation (DFG) in the framework of the excellence initiative.

REFERENCES

- [1] G. A. Johnson, A. Badea, J. Brandenburg, G. Cofer, B. Fubara, S. Liu, and J. Nissanov, "Waxholm space: An image-based reference for coordinating mouse brain research," *NeuroImage*, vol. 53, no. 2, pp. 365–372, Nov. 2010.
- [2] T. Ju, J. Warren, J. Carson, M. Bello, I. Kakadiaris, W. Chiu, C. Thaller, and G. Eichele, "3D volume reconstruction of a mouse brain from histological sections using warp filtering," *Journal of Neuroscience Methods*, vol. 156, no. 1-2, pp. 84–100, Sep. 2006.
- [3] Likar, Maintz, Viergever, and Pernu, "Retrospective shading correction based on entropy minimization," *Journal of Microscopy*, vol. 197, no. 3, pp. 285–295, 2000.
- [4] F. J. W.-M. Leong, M. Brady, and J. O. McGee, "Correction of uneven illumination (vignetting) in digital microscopy images," *J Clin Pathol*, vol. 56, no. 8, pp. 619–621, Aug. 2003.
- [5] G. Malandain and E. Bardin, "Intensity compensation within series of images," in *Medical Image Computing and Computer-Assisted Intervention - MICCAI 2003*, 2003, pp. 41–49.

- [6] J. Dauguet, J.-F. Mangin, T. Delzescaux, and V. Frouin, "Robust inter-slice intensity normalization using histogram scale-space analysis," in *Medical Image Computing and Computer-Assisted Intervention - MICCAI 2004*, 2004, pp. 242–249.
- [7] U. Bagci and L. Bai, "Registration of Standardized Histological Images in Feature Space," *ArXiv e-prints*, Jul. 2009.
- [8] O. Schmitt, J. Modersitzki, S. Heldmann, S. Wirtz, and B. Fischer, "Image registration of sectioned brains," *International Journal of Computer Vision*, vol. 73, no. 1, pp. 5–39, Jun. 2007.
- [9] J. Dauguet, T. Delzescaux, F. Condé, J.-F. Mangin, N. Ayache, P. Hantraye, and V. Frouin, "Three-dimensional reconstruction of stained histological slices and 3d non-linear registration with in-vivo MRI for whole baboon brain," *Journal of Neuroscience Methods*, vol. 164, no. 1, pp. 191–204, Aug. 2007.
- [10] J. Yelnik, E. Bardinet, D. Dormont, G. Malandain, S. Ourselin, D. Tandé, C. Karachi, N. Ayache, P. Cornu, and Y. Agid, "A three-dimensional, histological and deformable atlas of the human basal ganglia. i. atlas construction based on immunohistochemical and MRI data," *NeuroImage*, vol. 34, no. 2, pp. 618–638, Jan. 2007.
- [11] V. J. Dercksen, C. Brüß, D. Stalling, S. Gubatz, U. Seiffert, and H.-C. Hege, "Towards automatic generation of 3d models of biological objects based on serial sections," in *Visualization in Medicine and Life Sciences*, 2008, pp. 3–25.
- [12] G. Born, "Die Plattenmodellmethode," *Archiv für mikroskopische Anatomie*, vol. 22, no. 1, pp. 584–599, Dec. 1883.
- [13] A. Cifor, L. Bai, and A. Pitiot, "Smoothness-guided 3-D reconstruction of 2-D histological images," *NeuroImage*, vol. 56, no. 1, pp. 197–211, May 2011.
- [14] A. W. Toga, A. Goldkorn, K. Ambach, K. Chao, B. C. Quinn, and P. Yao, "Postmortem cryosectioning as an anatomic reference for human brain mapping," *Computerized Medical Imaging and Graphics*, vol. 21, no. 2, pp. 131–141, mar 1997.
- [15] C. F. Burgoyne, J. C. Downs, A. J. Bellezza, and R. T. Hart, "Three-dimensional reconstruction of normal and early glaucoma monkey optic nerve head connective tissues," *Invest. Ophthalmol. Vis. Sci.*, vol. 45, no. 12, pp. 4388–4399, Dec. 2004.
- [16] J. Dauguet, T. Delzescaux, F. Condé, J.-F. Mangin, N. Ayache, P. Hantraye, and V. Frouin, "Three-dimensional reconstruction of stained histological slices and 3d non-linear registration with in-vivo {MRI} for whole baboon brain," *Journal of Neuroscience Methods*, vol. 164, no. 1, pp. 191 – 204, 2007.
- [17] M. Feuerstein, H. Heibel, J. Gardiazabal, N. Navab, and M. Groher, "Reconstruction of 3-d histology images by simultaneous deformable registration," in *Medical Image Computing and Computer-Assisted Intervention (MICCAI) 2011*, ser. Lecture Notes in Computer Science, G. Fichtinger, A. Martel, and T. Peters, Eds. Springer Berlin Heidelberg, Jan. 2011, no. 6892, pp. 582–589.
- [18] P. A. Yushkevich, B. B. Avants, L. Ng, M. Hawrylycz, P. D. Burststein, H. Zhang, and J. C. Gee, "3D mouse brain reconstruction from histology using a coarse-to-fine approach," in *Biomedical Image Registration*, ser. Lecture Notes in Computer Science, J. P. W. Pluim, B. Likar, and F. A. Gerritsen, Eds. Springer Berlin Heidelberg, Jan. 2006, no. 4057, pp. 230–237.
- [19] G. Malandain, E. Bardinet, K. Nelissen, and W. Vanduffel, "Fusion of autoradiographs with an MR volume using 2-d and 3-d linear transformations," *NeuroImage*, vol. 23, no. 1, pp. 111–127, Sep. 2004.
- [20] U.-D. Braumann, J.-P. Kuska, J. Einenkel, L.-C. Horn, M. Löffler, and M. Hockel, "Three-dimensional reconstruction and quantification of cervical carcinoma invasion fronts from histological serial sections," *Medical Imaging, IEEE Transactions on*, vol. 24, no. 10, pp. 1286–1307, 2005.
- [21] S. Wirtz, B. Fischer, J. Modersitzki, and O. Schmitt, "Superfast elastic registration of histologic images of a whole rat brain for 3D reconstruction," in *Proc. SPIE Medical Imaging 2004: Image Proc.*, vol. 5370, 2004, pp. 328–334.
- [22] M. M. Chakravarty, G. Bertrand, C. P. Hodge, A. F. Sadikot, and D. L. Collins, "The creation of a brain atlas for image guided neurosurgery using serial histological data," *NeuroImage*, vol. 30, no. 2, pp. 359–376, Apr. 2006.
- [23] M. M. Chakravarty, B. J. Bedell, S. P. Zehntner, A. C. Evans, and D. L. Collins, "Three-dimensional reconstruction of serial histological mouse brain sections," in *5th IEEE International Symposium on Biomedical Imaging: From Nano to Macro, 2008. ISBI 2008*. IEEE, May 2008, pp. 987–990.
- [24] A. Pitiot, E. Bardinet, P. M. Thompson, and G. Malandain, "Piecewise affine registration of biological images for volume reconstruction," *Medical Image Analysis*, vol. 10, no. 3, pp. 465–483, Jun. 2006.
- [25] A. Pitiot and A. Guimond, "Geometrical regularization of displacement fields for histological image registration," *Medical Image Analysis*, vol. 12, no. 1, pp. 16–25, Feb. 2008.
- [26] U. Bagci and L. Bai, "Automatic best reference slice selection for smooth volume reconstruction of a mouse brain from histological images," *Medical Imaging, IEEE Transactions on*, vol. 29, no. 9, pp. 1688–1696, 2010.
- [27] P. Scheibe, T. Wetzig, J.-P. Kuska, M. Löffler, J. C. Simon, U. Paasch, and U.-D. Braumann, "3D-Reconstruction of basal cell carcinoma," in *Biomedical Image Registration*, B. Fischer, B. M. Dawant, and C. Lorenz, Eds. Berlin, Heidelberg: Springer Berlin Heidelberg, 2010, vol. 6204, pp. 25–36.
- [28] J. Streicher, W. J. Weninger, and G. B. Müller, "External marker-based automatic congruencing: A new method of 3D reconstruction from serial sections," *The Anatomical Record*, vol. 248, no. 4, pp. 583–602, 1997.
- [29] V. Daum, "Model-constrained non-rigid registration in medicine," Ph.D. dissertation, Friedrich-Alexander-Universität Erlangen-Nürnberg, 2012.
- [30] B. Fischer and J. Modersitzki, "Curvature based image registration," *Journal of Mathematical Imaging and Vision*, vol. 18, no. 1, pp. 81–85, 2003.
- [31] J. Modersitzki, *Numerical Methods for Image Registration*. Oxford: Oxford University Press, Dec. 2003.
- [32] S. Gaffling, V. Daum, and J. Hornegger, "Landmark-constrained 3-d histological imaging: A morphology-preserving approach." in *VMV*, P. Eisert, J. Hornegger, and K. Polthier, Eds. Eurographics Association, 2011, pp. 309–316.
- [33] H. R. Schwarz and N. Köckler, *Numerische Mathematik*. Springer, Deutschland, 2009.
- [34] W. L. Briggs, V. E. Henson, and S. F. McCormick, *A multigrid tutorial (2nd ed.)*. Philadelphia, PA, USA: Society for Industrial and Applied Mathematics, 2000.
- [35] L. Kohaupt, "Basis of eigenvectors and principal vectors associated with Gauss-Seidel matrix of a = tridiag [-1 2 -1]," *SIAM Review*, vol. 40, no. 4, pp. 959–964, Dec. 1998.
- [36] S. Gaffling, F. Jäger, V. Daum, M. Tauchi, and E. Lütjen-Drecoll, "Interpolation of histological slices by means of non-rigid registration," in *Bildverarbeitung für die Medizin 2009*, 2009, pp. 267–271.
- [37] "Digimorph staff - Zaedyus pichiy," May 2012. [Online]. Available: http://www.digimorph.org/specimens/Zaedyus_pichiy/whole
- [38] J. Fitzpatrick, J. West, and J. Maurer, C.R., "Predicting error in rigid-body point-based registration," *IEEE Transactions on Medical Imaging*, vol. 17, pp. 694–702, Oct. 1998.
- [39] S. Baheerathan, F. Albrechtsen, and H. Danielsen, "Registration of serial sections of mouse liver cell nuclei," *Journal of Microscopy*, vol. 192, no. 1, pp. 37–53, 1998.
- [40] E. Guest and R. Baldock, "Automatic reconstruction of serial sections using the finite element method," *Bioimaging*, vol. 3, no. 4, pp. 154–167, 1995.
- [41] R. Haralick, K. Shanmugam, and I. Dinstein, "Textural features for image classification," *IEEE Transactions on Systems, Man and Cybernetics*, vol. SMC-3, no. 6, pp. 610–621, Nov. 1973.
- [42] D. Rueckert, L. I. Sonoda, C. Hayes, D. L. G. Hill, M. O. Leach, and D. Hawkes, "Nonrigid registration using free-form deformations: application to breast mr images," *Medical Imaging, IEEE Transactions on*, vol. 18, no. 8, pp. 712–721, Aug 1999.
- [43] L. Ibanez, W. Schroeder, L. Ng, and J. Cates, *The ITK Software Guide*, 2nd ed., Kitware, Inc., 2005, ISBN 1-930934-15-7. [Online]. Available: <http://www.itk.org/ItkSoftwareGuide.pdf>
- [44] K. B. J. Franklin and G. Paxinos, *The mouse brain in stereotaxic coordinates*. San Diego: Academic Press, 1997.
- [45] L. Kindle, I. Kakadiaris, T. Ju, and J. Carson, "A semiautomated approach for artefact removal in serial tissue cryosections," *Journal of Microscopy*, vol. 241, no. 2, pp. 200–206, Feb. 2011.
- [46] V. Kaynig, B. Fischer, and J. Buhmann, "Probabilistic image registration and anomaly detection by nonlinear warping," in *Computer Vision and Pattern Recognition, 2008. CVPR 2008. IEEE Conference on*, 2008, pp. 1–8.
- [47] P. Risholm, E. Samsø, I.-F. Talos, and W. Wells, "A non-rigid registration framework that accommodates resection and retraction," in *Information Processing in Medical Imaging*, ser. Lecture Notes in Computer Science, J. L. Prince, D. L. Pham, and K. J. Myers, Eds. Springer Berlin Heidelberg, Jan. 2009, no. 5636, pp. 447–458.